How to cite: *Angew. Chem. Int. Ed.* **2025**, *64*, e202501169
doi.org/10.1002/anie.202501169

Polycycles

A Key Fragment in Carbon Schwarzite Unit Cells and Its Triple [6]Helicene Precursor

*Xinhe Yang, Shilong Su, Chenyu Hu, Ka Man Cheung, Daiyue Yang, Xiao Chen, Jun Yang, Zhifeng Huang, Fuk Yee Kwong, and Qian Miao**

Abstract: This study explores two structurally related π-skeletons. The π-skeleton of compounds **1a–e** containing three heptagons represents a key fragment in theoretical carbon schwarzites, while that of **2a–b** is a triple [6]helicene. Compounds **1a–e** were synthesized via Scholl reactions, and using a weaker acid allowed the reaction to stop at an intermediate stage, yielding **2a–b**. X-ray crystallography revealed not only distinct stereochemistry of **1b** and **2a** but also unique supramolecular assemblies in the clathrate of **2a** with chloroform. Compound **1b** adopts a saddle-like geometry, while **2a** exhibits a propeller-like structure with C_3 symmetry, consistent with density functional theory (DFT) calculations. The π-skeleton of **1a–e** is flexible, enabling rapid enantiomerization, whereas that of **2a–b** is rigid, allowing resolution of **2b** into optically pure forms with an absorption dissymmetry factor as high as 0.015. Comparative analysis shows that presence of seven-membered rings in **1a–e** does not significantly alter the local aromaticity of the triple [6]helicene framework.

Introduction

Carbon schwarzites, also known as Mackay crystals, are theoretical allotropes of sp^2-hybridized carbon characterized by negative curvature. These names honor A. L. Mackay and H. Schwarz, respectively. Mackay first proposed the concept of negatively curved carbon allotropes by incorporating octagons into the graphitic lattice in 1991,[1] while Schwarz described triply periodic minimal surfaces, the topological model for Mackay crystals, in the 1880s. Curvature is a geometric property describing the overall feature of the surfaces formed by carbon atoms. The negative curvature in carbon schwarzites is induced by seven or eight-membered rings embedded in the graphitic lattice, whereas positive curvature in fullerenes are induced by five-membered rings. Despite predictions of their intriguing properties and potential applications,[2,3] carbon schwarzites have not yet been synthesized unambiguously. The closest approximations to carbon schwarzites so far are 3D graphene-like carbons formed using a zeolite template.[4,5] Fragments of carbon schwarzites that retain their structural characteristics are negatively curved polycyclic arenes.[6,7] These fragments are 3D molecular nanocarbons that include heptagons,[8–10] octagons,[11–14] or even larger carbocycles. In principle, negatively curved polycyclic arenes could serve as building blocks in a bottom-up approach to constructing carbon schwarzites.[15–17] To support this idea, we recently demonstrated that polymerizing negatively curved polycyclic arenes resulted in an amorphous covalent network. This network was able to mimic the structure and function of carbon schwarzites to a certain degree, serving as a high-capacity anode material in lithium-ion batteries.[18] Further advancements in the bottom-up approach to carbon schwarzites will require the synthesis of new negatively curved polycyclic arenes containing multiple heptagons[19–21] or octagons and their subsequent expansion into larger 3D molecular nanocarbons. As shown in Figure 1, polycyclic arenes **1a–e**, containing three heptagons, are a key fragment in different carbon schwarzite unit cells. This study presents the synthesis of **1a–e** using Scholl reactions with triple [6]helicene **2a–b** as intermediates, compares the stereochemistry,

[*] X. Yang
State Key Laboratory of Antiviral Drugs, Pingyuan Laboratory, School of Chemistry and Chemical Engineering, Henan Normal University, Xinxiang, Henan 453007, China

X. Yang
Shanghai-Hong Kong Joint Laboratory in Chemical Synthesis, Shanghai Institute of Organic Chemistry, Chinese Academy of Sciences, Shanghai 230032, China

S. Su, K. M. Cheung, D. Yang, X. Chen, Z. Huang, F. Y. Kwong, Q. Miao
Department of Chemistry, The Chinese University of Hong Kong, Shatin, Hong Kong, New Territories, China
E-mail: miaoqian@cuhk.edu.hk

Q. Miao
Shanghai-Hong Kong Joint Laboratory in Chemical Synthesis, The Chinese University of Hong Kong, Shatin, Hong Kong, New Territories, China

C. Hu, J. Yang
Department of Chemistry, The University of Hong Kong, Hong Kong, China

Additional supporting information can be found online in the Supporting Information section

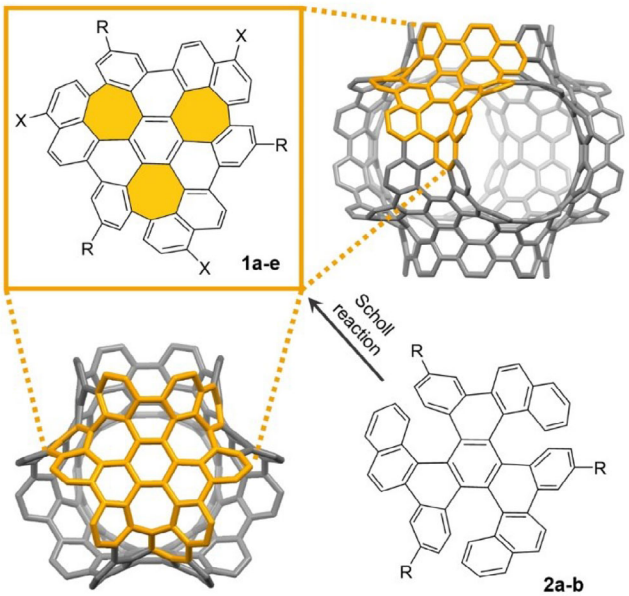

Figure 1. Structures of compounds **1a–e** and **2a–b** and the polycyclic skeleton of **1a–e** as mapped on carbon schwarzite unit cells.

aromaticity, and electronic properties of the two related π-skeletons of **1a–e** and **2a–b**, and highlights the supramolecular assemblies in the clathrate crystal of **2a** • $(CHCl_3)_2$.

Results and Discussion

As shown in Scheme 1, compounds **1a** and **1b** were synthesized through Suzuki coupling and Scholl reactions. Two pairs of coupling partners were tested in the triple Suzuki coupling reaction: 2-aryl-1-bromonaphthalene (**3a/b**) with benzene-1, 3, 5-triboronic acid (**4**), and 2-aryl-1-naphthaleneboronic acid (**5a/b**) with 1, 3, 5-tribromobenzene (**6**). Compounds **3a/b** were prepared via copper catalyzed [4 + 2] benzannulation of *o*-alkynylbenzaldehyde with alkynes[22] by modifying the reported procedures, [23] and compounds **5a/b** were prepared from **3a/b** through lithium-halogen exchange followed by borylation, as detailed in the Supporting Information. The reaction conditions, including phosphine ligands and bases, were optimized. It was found that using $Pd(dppf)Cl_2$ and K_3PO_4 in a mixed solvent of DMF and H_2O (2:1) at 100 °C provided the highest yields of triarylbenzene (**7a/b**) from both pairs of coupling partners. Under these optimized conditions, compound **7b** was obtained in a higher yield than **7a**, presumably due to the increased solubility of the starting material and intermediates provided by the *t*-butyl groups. The Scholl reactions of **7a** and **7b** with 9.0 equivalents of 2, 3-dichloro-5, 6-dicyano-1, 4-benzoquinone (DDQ) and CH_3SO_3H led to the formation of triple [6]helicenes **2a** and **2b**, respectively, with three new C–C bonds formed. Further treatment of compounds **2a/b** with 9.0 equivalents of DDQ and triflic acid resulted in compounds **1a/b**, which feature three seven-membered rings as a result of forming additional C–C bonds between the terminal rings of the [6]helicene moieties. Additionally, three triflate groups were attached to the

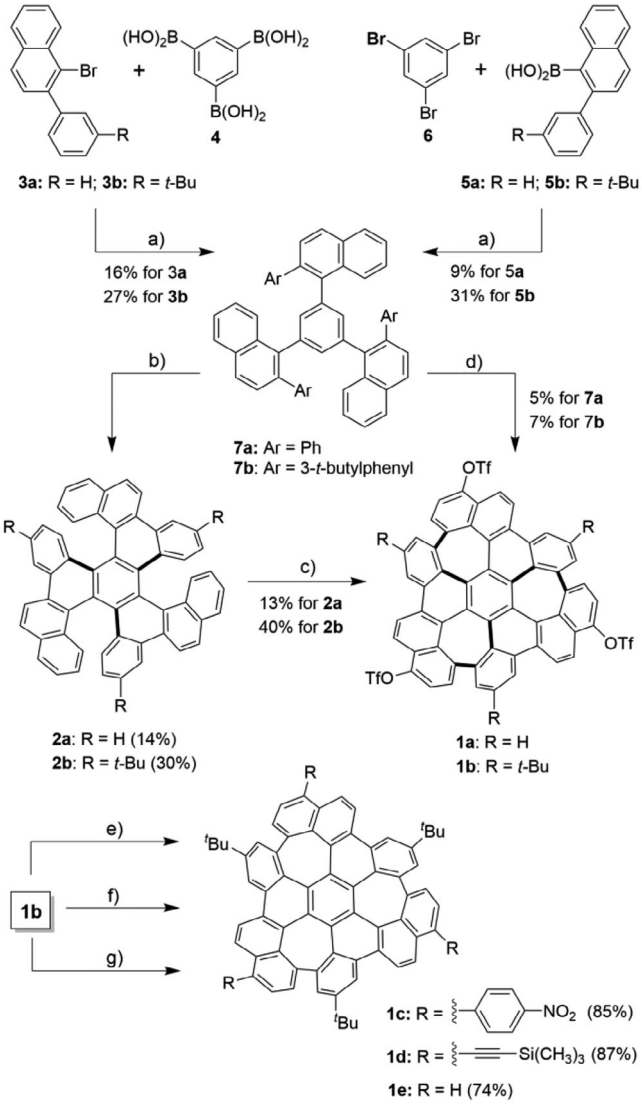

Scheme 1. Synthesis of **1a–e** and **2a–b**. Reagents and conditions: a) $Pd(dppf)Cl_2$, K_3PO_4, DMF/H_2O (2:1), 100 °C; b) DDQ (9.0 eq.), CH_3SO_3H, CH_2Cl_2, r.t.; c) DDQ (9.0 eq.), TfOH, CH_2Cl_2, rt; d) DDQ (9.0 eq.), TfOH, CH_2Cl_2, rt; e) $Pd(PPh_3)_4$, K_2CO_3, toluene/EtOH/H_2O (2:1:1), 80 °C; f) $Pd(PPh_3)_2Cl_2$, CuI, Et_3N, DMF, 80 °C; g) $Pd(OAc)_2$, PPh_3, Et_3N, HCO_2H, DMF, 65 °C (dppf = 1,1′-bis(diphenylphosphino) ferrocene, Tf = trifluomethanesulfonyl).

naphthalene moieties, positioned *para* to the newly formed C–C bonds, similar to previously reported incorporations of triflate[24] or methanesulfonate[25] groups in Scholl reaction products. In comparison, direct treatment of **7a/b** with 9.0 equivalents of DDQ and triflic acid resulted in the formation of compounds **1a** and **1b** as the only isolable products, with low yields of 5% and 7%, respectively. In these Scholl reactions, the *t*-butylated products (**2b** and **1b**) were obtained in higher yields than **2a** and **1a**, respectively, likely due to the increased solubility of the starting materials, intermediates, and products provided by the *t*-butyl groups. The low yields observed in these Scholl reactions can be attributed to the formation of incompletely cyclized products, which exhibited smaller R_f values compared to the target products on the

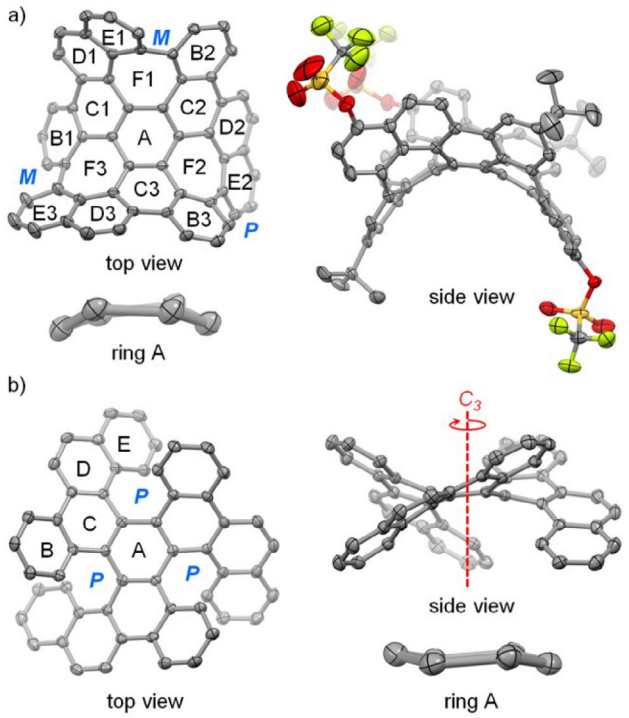

Figure 2. a) Structures of (*P*,*M*,*M*)-**1b** in the crystal of **1b** with rings labeled; b) structures of (*P*,*P*,*P*)-**2a** in the crystal of **2a** • $(CHCl_3)_2$ with rings labeled. (C, S, O and F atoms are shown as ellipsoids at 50% probability level, substituting groups in the top view, H atoms and disordered atoms are removed for clarification).

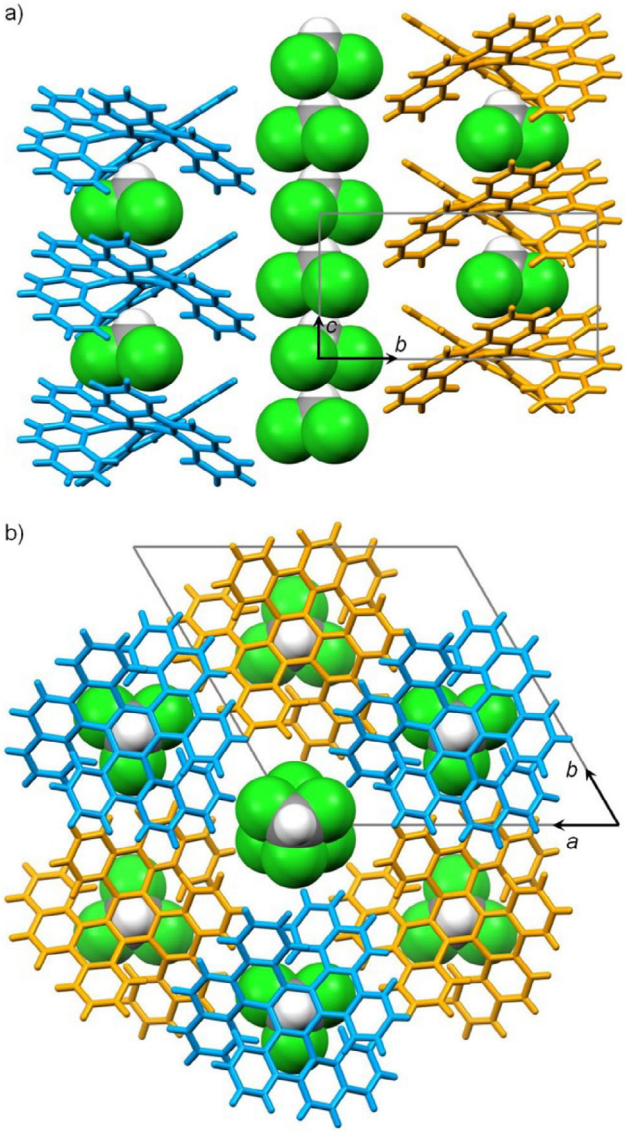

Figure 3. Supramolecular assemblies in the crystal of **2a** • $(CHCl_3)_2$ as viewed along the *a* axis a) and the *c* axis b) of unit cell, where (*P*,*P*,*P*)-**2a**) and (*M*,*M*,*M*)-**2a** are shown in orange and blue, respectively.

thin-layer chromatography (TLC) plate. These by-products were identified using mass spectrometry. Although some of them could be isolated in a relatively pure form, their complex ^{1}H NMR spectra made structural determination very challenging. Additionally, other by-products were observed at the baseline of TLC plates, likely resulting from polymerization through intermolecular oxidative coupling. The π-skeletons of **1b** were further extended by Suzuki coupling and Sonogashira coupling reactions, yielding compounds **1c** and **1d** in very good yields, respectively. In addition, Pd-catalyzed desulfonation of **1b** using formic acid resulted in compound **1e** in a yield of 74%.

Single crystals of compounds **1b**, **2a** and **2b** were obtained through slow evaporation of their solutions in CH_2Cl_2/hexane or chloroform. As revealed by X-ray crystallography[26] analysis, the polycyclic skeleton of **1b** has a saddle-like shape, while that of **2a** resembles a propeller with C_3 symmetry, as shown in Figure 2. The C_3 axis of **2a** is depicted in the side view in Figure 2b. The polycyclic skeleton of **2b** exhibiting approximate C_3 symmetry is essentially the same as that of **2a**. Compounds **1b** and **2a** are both chiral molecules, existing as pairs of enantiomers in the racemic crystals. Each seven-membered ring in **1b** is surrounded by a [6]helicene moiety, forming a hexa[7]circulene unit, which exhibits helicity similar to [6]helicene. According to the helicities of the three hexa[7]circulene units, the two enantiomers of **1b** in the crystal are (*P*,*M*,*M*)-**1b** and (*M*,*P*,*P*)-**1b**. In contrast, compound **2a** in the crystal exhibits the same helicity in its three [6]helicene moieties, existing as (*P*,*P*,*P*)-**2a** and (*M*,*M*,*M*)-**2a**. The central benzenoid rings (ring A) in **1b** and **2a** are the most contorted among all the benzenoid rings but exhibit different shapes. Ring A in **1b** adopts a boat geometry with torsion angles ranging widely from 7.4° to 31.5°, whereas that in **2a** adopts a chair geometry with torsion angles of 18.6° and 18.7°.

An interesting finding from the crystal structure of **2a** • $(CHCl_3)_2$ is the formation of unique supramolecular assemblies. In this crystal, co-crystallized chloroform molecules are imprisoned in the network of **2a**, forming a clathrate. As shown in Figure 3a, molecules of **2a** with the same helicity align themselves into segregated columns, with a chloroform molecule nestled between two neighboring **2a** molecules within each column. These columns further assemble into a hexagonal lattice, as shown in Figure 3b. Remarkably,

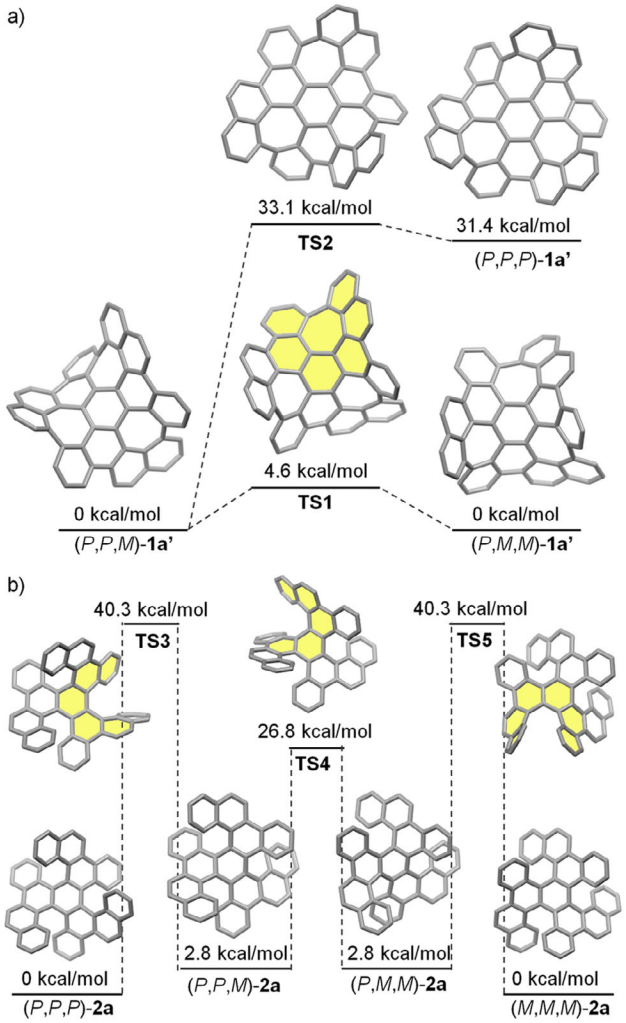

Figure 4. Stereoisomerization of **1a**′ a) and **2a** b) with relative Gibbs free energy calculated at the B3LYP/6-31G(d) level of DFT.

the spaces between these columns are filled by chloroform molecules, which form their own supramolecular columns. Two neighboring chloroform molecules exhibit three short intermolecular H-to-Cl contacts, each at a distance of 2.98 Å. To the best of our knowledge, such supramolecular columns of chloroform within a clathrate crystal represent a novel structural motif not previously documented in the literature.

To investigate the stereochemistry of the π-framework of **1a–e** and **2a–b**, Density functional theory (DFT) calculations were conducted at the B3LYP/6-31G(d) level using **2a** and **1a**′, which has hydrogen atoms replacing all the triflate groups in **1a**. Geometry optimization reveals that **1a**′ adopts a horse saddle-shaped geometry at the global minima, existing as a pair of enantiomers, (*P*,*P*,*M*)-**1a**′ and (*P*,*M*,*M*)-**1a**′, as illustrated in Figure 4a. The structures of (*P*,*P*,*M*)-**1a**′ and (*P*,*M*,*M*)-**1a**′ align well with the polycyclic skeleton of **1b** found in the crystal. The interconversion of the two enantiomers occurs through the transition state TS1 mainly involving the conformational change in the yellow hexa[7]circulene moiety. This transition state has an energy barrier as low as 4.6 kcal mol^{-1}, corresponding to a rate as high as 2.6×10^9 at 25 °C, as estimated using the Eyring equation and assuming a value of unity for the transmission coefficient. This energy barrier for enantiomerization is lower than that of hexa[7]circulene (16 kcal mol^{-1}).[19] On the other hand, molecule **1a**′ adopts a monkey saddle-shaped geometry with a C_3 symmetry at local minima, existing as a pair of enantiomers, (*P*,*P*,*P*)-**1a**′ and (*M*,*M*,*M*)-**1a**′, which are significantly higher in Gibbs free energy than their diastereomers, (*P*,*P*,*M*)-**1a**′ and (*P*,*M*,*M*)-**1a**′, by 31.4 kcal mol^{-1}. The transition state (TS2) between (*P*,*P*,*M*)-**1a**′ and (*P*,*P*,*P*)-**1a**′ is close to (*P*,*P*,*P*)-**1a**′ in both geometry and energy. As a result, the C3-symmetric structure of **1a**′ is unfavorable both thermodynamically and kinetically. The three-fold symmetry observed in the NMR spectra of **1a–e** should therefore attributed to rapid interconversion between (*P*,*P*,*M*)-**1a**′ and (*P*,*M*,*M*)-**1a**′, resulting in an average structure of three-fold symmetry. Unlike **1a**′, triple [6]helicene **2a** adopts a propeller-shaped geometry with a C_3 symmetry at the global minima, existing as a pair of enantiomers, (*P*,*P*,*P*)-**2a** and (*M*,*M*,*M*)-**2a** (Figure 4b), in agreement with the polycyclic skeleton of **2a** in the crystal. Meanwhile, the other stereoisomers, (*P*,*P*,*M*)-**2a** and (*P*,*M*,*M*)-**2a**, are found at local minima and are higher in Gibbs free energy by 2.8 kcal mol^{-1}. The enantiomerization of (*P*,*P*,*P*)-**2a** to (*M*,*M*,*M*)-**2a** involves (*P*,*P*,*M*)-**2a** and (*P*,*M*,*M*)-**2a** as intermediates and proceeds through three transition states (TS3–5). Each transition state primarily involves a conformational change in one hexa[7]circulene moiety (colored in yellow), with an energy barrier as high as 40.3 kcal mol^{-1} for TS3. Therefore, (*P*,*P*,*P*)-**2a** to (*M*,*M*,*M*)-**2a** is rigid, making these enantiomers enantiostable.[27]

The aromaticity of the π-backbones in compounds **1a–e** and **2a–b** was evaluated using two methods: the Harmonic Oscillator Model of Aromaticity (HOMA)[28,29] and Nucleus Independent Chemical Shift (NICS).[30] HOMA assesses aromaticity by bond length equalization based on crystal structure data, whereas NICS evaluates ring currents via DFT calculations. For NICS(1) analysis, ghost atoms were positioned above and below the curved faces of compounds **1a**′ and **2a**, yielding NICS(1) and NICS(−1) values for each ring. The ring labels are detailed in Figures 2, with the corresponding HOMA and NICS results summarized in Table 1. Despite lacking three-fold symmetry, rings within the π-backbones of **1b** and **1a**′—excluding the central benzenoid ring—can be categorized into three sets (labeled 1–3), each containing rings B through F. Rings sharing the same letter typically exhibit similar HOMA values, except for ring E3, which contains disordered carbon atoms leading to greater uncertainty in bond lengths. Among the six-membered rings in **1b**, C1–3 have the lowest HOMA values, consistent with Clar's aromatic sextet rule predicting reduced aromaticity. Ring A has a low HOMA value of 0.532, contrary to expectations from Clar's rule, due to its distorted geometry as depicted in Figure 2a.

These findings correlate with the negative NICS values of small magnitude observed in the corresponding rings in **1a**′. The seven-membered rings (F1–3) display near-zero HOMA values, suggesting nonaromatic character. Accordingly, these rings in **1a**′ show minor positive NICS values, which indicate

Table 1: HOMA values in different rings of **1b** and **2a** and NICS values for different rings in **1a**′ and **2a**.

Ring in 1b or 1a′[a]	HOMA[b]	NICS(1) (ppm)[c]	NICS(−1) (ppm)[c]
A	0.532	−6.478	−7.065
B1	0.921	−9.022	−8.195
B2	0.878	−10.574	−9.680
B3	0.930	−9.137	−10.934
C1	0.299	−5.545	−6.388
C2	0.307	−5.493	−7.321
C3	0.291	−7.843	−4.806
D1	0.573	−12.128	−8.073
D2	0.566	−8.324	−10.129
D3	0.571	−8.422	−9.136
E1	0.846	−9.469	−10.008
E2	0.835	−11.497	−9.919
E3	0.651	−9.981	−10.744
F1	−0.166	3.581	2.422
F2	−0.155	2.576	3.105
F3	0.013	3.914	4.678

Ring in **2a**[a]	HOMA	NICS(1) (ppm)[c]	NICS(−1) (ppm)[c]
A	0.564	−4.057	−7.360
B	0.926	−10.157	−11.633
C	0.261	−4.349	−5.277
D	0.615	−10.163	−7.814
E	0.810	−12.634	−11.222

[a] Labeling of the rings are shown in Figure 2; [b] HOMA = $1-(\alpha/n)\Sigma(R_{opt}-R_i)^2$, where n is the number of bonds taken into the summation, $\alpha = 257.7$ is an empirical constant chosen to give HOMA = 0 for the hypothetical Kekulé structures with alternation of single and double bonds and HOMA = 1 for the system with all bond lengths equal to the optimal value $R_{opt} = 1.388$ Å, and R_i is the individual bond length in the ring; [c] Calculated at the B3LYP/6-31G(d,p) level of DFT using the standard GIAO method.

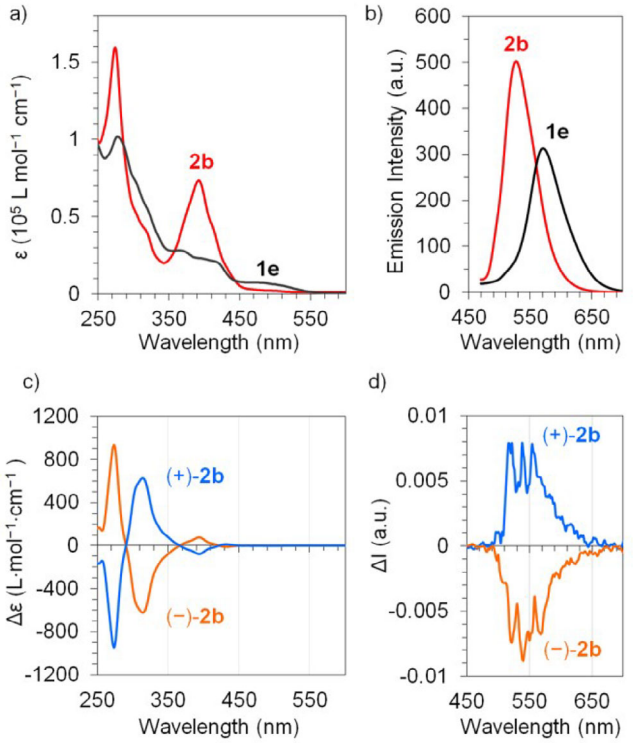

Figure 5. a) UV-vis absorption of **1e** and **2b** in CH_2Cl_2 (5×10^{-6} mol/L); b) photoluminescence spectra of **1e** and **2b** in CH_2Cl_2 (5×10^{-6} mol/L) as excited as 442 nm, respectively; c) CD spectra of **2b** in CH_2Cl_2 (1×10^{-5} mol/L); d) CPL spectra of **2b** CH_2Cl_2 (1×10^{-5} mol/L) as excited at 395 nm.

neither inherent aromatic nor antiaromatic character but rather reflect the deshielding effects from adjacent aromatic rings. The HOMA values and NICS values for **2a** are summarized in Table 1 according to five rings (A–E). This organization reflects that **2a** possesses C3 symmetry. Both metrics indicate that relative aromaticity follows the order of B ≈ E > A ≈ D > C, a pattern also seen in **1b** and **1a**′. This can be explained by the presence of Clar's aromatic sextets on rings B and E and the contorted nature of ring A. Overall, forming seven-membered rings in **1a–e** does not significantly alter the local aromaticity of the triple [6]helicene framework.

To compare the electronic properties of the two related π-skeletons in compounds **1a–e** and **2a–b**, we selected **1e** and **2b** due to their identical tert-butyl substituents, which exert minimal influence on the electronic structures. The electrochemical properties of **1e** and **2b** were investigated using cyclic voltammetry (CV), while their optical properties were characterized by UV-vis absorption, photoluminescence, circular dichroism (CD), and circularly polarized luminescence (CPL) spectroscopy. In the CV test window, both **1e** and **2b** exhibit one pseudo-reversible oxidation wave and one reversible oxidation wave (Figures S40 and S41 in the Supporting Information). The first oxidation potentials of **1e** and **2b** are 0.18 and 0.20 V versus ferrocenium/ferrocene, respectively, based on which the highest occupied molecular orbital (HOMO) energy levels for **1e** and **2b** are estimated at −5.28 eV and −5.30 eV, respectively, based on a formal potential of −5.10 eV for ferrocenium/ferrocene in the Fermi scale.[31] These values are close to the DFT-calculated HOMO energy levels (−5.06 eV for 1′ and −5.37 eV for 2′). Figure 5a compares the absorption spectra of **1e** and **2b**, and Figure 5b compares the emission spectra of **1e** and **2b** when excited at 442 nm, a wavelength where both compounds have the same molar extinction coefficient. Both **1e** and **2b** are weakly fluorescent with absolute fluorescence quantum yields of 2.3% and 1.9%, respectively. The rigid triple [6]helicene framework of **2b** allowed it to be resolved into two enantiomers, (*P*,*P*,*P*)-**2b** and (*M*,*M*,*M*)-**2b**. As shown in Figure 5c, optically pure forms of **2b** exhibit significant electronic circular dichroism primarily in the UV region. Compound **2b** shows maximum $|\Delta\varepsilon|$ values of 947 L·mol^{-1}·cm^{-1} at 274 nm, 626 L·mol^{-1}·cm^{-1} at 314 nm and 78 L mol^{-1}·cm^{-1} at 394 nm. The corresponding absorption dissymmetry factors, $g_{abs} = |\Delta\varepsilon|/\varepsilon$, are calculated as 5.9×10^{-3} at 274 nm, 1.5×10^{-2} at 314 nm and 1.1×10^{-3} at 394 nm. Notably, the g_{abs} value of 1.5×10^{-2} is larger than most reported chiral organic dyes (typically in the order of 10^{-3}) and ranks among the highest values observed for multiple helicenes[32–36] and helical multilayer nanographenes[37–39] (in the order of 10^{-2}). The optically pure forms of **2b** also exhibit circularly polarized luminescence (CPL) activity within the wavelength range of 500 to 650 nm (Figure 5d), with the luminescence

dissymmetry factor (g_{lum}) reaching 2.2 × 10^{-3} (Figure S36). For context, the g_{lum} values for typical organic circularly polarized emitters are generally on the order of 10^{-3}.[40]

To better understand the observed photophysical, particularly, chiroptical properties of **2b**, time-dependent density functional theory (TDDFT) calculations were performed at the B3LYP-D3(BJ)/6-31G(d,p) level of the theory. The theoretical analysis indicated that the $S_0 \rightarrow S_1$ electronic transition occurs at 471 nm with an oscillator strength of 3 × 10^{-4}, aligning well with the experimentally observed weak absorption band in the range of 450 to 510 nm. Similarly, the $S_1 \rightarrow S_0$ transition at 528 nm exhibits an oscillator strength of 2 × 10^{-4}, consistent with the low absolute fluorescence quantum yield of **2b**. The simulated electronic circular dichroism (ECD) spectrum of **2b** (Figure S32) shows good agreement with experimental results. In particular, the significant $|\Delta\varepsilon|$ value at 314 nm in the CD spectra of (+) and (−)-**2b** can be attributed to the $S_0 \rightarrow S_{20}$, $S_0 \rightarrow S_{21}$, $S_0 \rightarrow S_{22}$ and $S_0 \rightarrow S_{23}$ transitions (Table S1), with the calculated absolute values of dissymmetry factors ranging from 0.054 to 0.081. These values are compatible with the experimentally observed high dissymmetry factor of 0.015. The dissymmetry factor (g) is determined by electric (μ) and magnetic (m) transition dipole moments through the equation $g = 4|\mu|\bullet|m| \cos\theta / (\mu^2 + m^2)$, where θ represents the angle between μ and m.[32,33] The high dissymmetry factor observed can be attributed to the near 180° angles between μ and m for these transitions (Table S1 and Figure S33). The observed g_{abs} and g_{lum} values differ significantly as they correspond to different electronic transitions. The observed lower g_{lum} value may be attributed to the weak fluorescence of **2b**, which results from the small oscillator strength (proportional to μ^2) for its $S_1 \rightarrow S_0$ transition.

Conclusion

In conclusion, this study puts forth a series of novel polycyclic arenes featuring two structurally related π-skeletons. Compounds **1a–e**, which contain three heptagons, represent a key fragment in carbon schwarzites, while compounds **2a–b** are triple [6]helicene derivatives. Compounds **1a** and **1b**, featuring triflate groups, were successfully synthesized from triarylbenzene (**7a/b**) via Scholl reactions using DDQ and triflic acid. By employing a weaker acid (CH_3SO_3H) to replace triflic acid, the Scholl reaction was controlled to halt at an intermediate stage, yielding **2a–b**. Utilizing the triflate groups, compound **1b** was further transformed into compounds **1c–e** through Pd-catalyzed coupling and desulfonation reactions. X-ray crystallography revealed that the polycyclic skeleton of **1b** adopts a saddle-like shape, while that of **2a** resembles a propeller with C_3 symmetry. Notably, **2a** co-crystallized with chloroform to form a clathrate, presenting unique supramolecular assemblies including a supramolecular column of chloroform molecules. The observed molecular geometries are consistent with DFT calculations, which indicate that horse saddle-shaped (*P*,*P*,*M*)-**1a**′ and (*P*,*M*,*M*)-**1a**′ are energetically favored as global minima, whereas monkey saddle-shaped (*P*,*P*,*P*)-**1a**′ and (*M*,*M*,*M*)-**1a**′ are thermodynamically and kinetically unfavorable. Furthermore, compounds **1a–e** exhibit a flexible π-skeleton that rapidly enantiomerizes, while compounds **2a–b** possess a rigid π-skeleton, allowing for resolution into optically pure forms. The optically pure **2b** exhibits an absorption dissymmetry factor as high as 0.015, one of the highest values reported for multiple helicenes. Comparative analysis of the electronic properties and aromaticity of the π-skeletons in **1a–e** and **2a–b**, using both computational and experimental methods, revealed that the introduction of seven-membered rings in **1a–e** does not significantly alter the local aromaticity of the triple [6]helicene framework.

Acknowledgements

We thank Dr. Xuebing Leng (Shanghai Institute of Organic Chemistry) for the single crystal crystallography. This research was supported by the Research Grants Council of Hong Kong (CRF C4001-23G and JLFS/P-404/24).

Conflict of Interests

The authors declare no conflict of interest.

Data Availability Statement

The data that support the findings of this study are available in the supplementary material of this article.

Keywords: Arenes · Clathrate · Polycycles · Stereochemistry

[1] A. L. Mackay, H. Terrones, *Nature* **1991**, *352*, 762.
[2] S. Park, K. Kittimanapun, J. S. Ahn, Y. K. Kwon, D. Tománek, *J. Phys.: Condens. Matter* **2010**, *22*, 334220.
[3] N. Park, M. Yoon, S. Berber, J. Ihm, E. Osawa, D. Tománek, *Phys. Rev. Lett.* **2003**, *91*, 237204.
[4] K. Kim, T. Lee, Y. Kwon, Y. Seo, J. Song, J. K. Park, H. Lee, J. Y. Park, H. Ihee, S. J. Cho, R. Ryoo, *Nature* **2016**, *535*, 131–135.
[5] E. Braun, Y. Lee, S. M. Moosavi, S. Barthel, R. Mercado, I. A. Baburin, D. M. Proserpio, B. Smit, *Proc. Natl. Acad. Sci. USA* **2018**, *115*, E8116.
[6] G. G. Miera, S. Matsubara, H. Kono, K. Murakami, K. Itami, *Chem. Sci.* **2022**, *13*, 1848–1868.
[7] Chaolumen, I. A. Stepek, K. E. Yamada, H. Ito, K. Itami, *Angew. Chem. Int. Ed.* **2021**, *60*, 23508–23532.
[8] K. Kawasumi, Q. Zhang, Y. Segawa, L. T. Scott, K. Itami, *Nat. Chem.* **2013**, *5*, 739–744.
[9] K. Y. Cheung, X. Xu, Q. Miao, *J. Am. Chem. Soc.* **2015**, *137*, 3910–3914.
[10] C. M. Cruz, I. R. Márquez, S. Castro-Fernández, J. M. Cuerva, E. Maçôas, A. G. Campaña, *Angew. Chem. Int. Ed.* **2019**, *58*, 8068–8072.
[11] Y. Sakamoto, T. Suzuki, *J. Am. Chem. Soc.* **2013**, *135*, 14074–14077.
[12] C.-N. Feng, M.-Y. Kuo, Y.-T. Wu, *Angew. Chem. Int. Ed.* **2013**, *52*, 7791–7794.
[13] K. Y. Cheung, C. K. Chan, Z. Liu, Q. Miao, *Angew. Chem. Int. Ed.* **2017**, *56*, 9003–9007.

[14] H. Pun, Y. Wang, M. Chu, C. K. Chan, Y. Li, Z. Liu, Q. Miao, *J. Am. Chem. Soc.* **2019**, *141*, 9680–9686.
[15] S. H. Pun, Q. Miao, *Acc. Chem. Res.* **2018**, *51*, 1630–1642.
[16] T. Kirschbaum, F. Rominger, M. Mastalerz, *Angew. Chem. Int. Ed.* **2020**, *59*, 270–274.
[17] M.-W. Wang, Z. Li, Y. Liu, W. Jiang, Z. Wang, *Org. Chem. Front.* **2023**, *10*, 2808–2812.
[18] Y. Zhang, Y. Zhu, D. Lan, S. H. Pun, Z. Zhou, Z. Wei, Y. Wang, H. K. Lee, C. Lin, J. Wang, M. A. Petrukhina, Q. Li, Q. Miao, *J. Am. Chem. Soc.* **2021**, *143*, 5231–5238.
[19] K. M. Cheung, Y. Xiong, S. H. Pun, X. Zhuo, Q. Gong, X. Zeng, S. Su, Q. Miao, *Chem* **2023**, *9*, 2855–2868.
[20] S. M. Elbert, O. T. Paine, T. Kirschbaum, M. P. Schuldt, L. Weber, F. Rominger, M. Mastalerz, *J. Am. Chem. Soc.* **2024**, *146*, 27324–27334.
[21] B. Borrisov, G. M. Beneventi, Y. Fu, Z.-L. Qiu, H. Komber, Q.-S. Deng, P. M. Greißel, A. Cadranel, D. M. Guldi, J. Ma, X. Feng, *J. Am. Chem. Soc.* **2024**, *146*, 27335–27344.
[22] N. Asao, T. Nogami, S. Lee, Y. Yamamoto, *J. Am. Chem. Soc.* **2003**, *125*, 10921–10925.
[23] R. Umeda, R. Ueda, T. Tanaka, A. Hayashi, M. Ikeshita, S. Suzuki, T. Naota, Y. Nishiyama, *Tetrahedron* **2021**, *79*, 131872.
[24] X. Yang, M. Hoffmann, F. Rominger, T. Kirschbaum, A. Dreuw, M. Mastalerz, *Angew. Chem. Int. Ed.* **2019**, *58*, 10650–10654.
[25] Y. Yang, L. Yuan, B. Shan, Z. Liu, Q. Miao, *Chem. – A Eur. J.* **2016**, *22*, 18620–18627.
[26] Deposition numbers 2415304, 2416279 and 2415305 contain the supplementary crystallographic data for **1b**, **2a** • $(CHCl_3)_2$, and **2b** • CH_2Cl_2, respectively. These data are provided free of charge by the joint Cambridge Crystallographic Data Centre and Fachinformationszentrum Karlsruhe Access Structures service.
[27] J. M. Fernández-García, P. Izquierdo-García, M. Buendía, S. Filippone, N. Martín, *Chem. Comm.* **2022**, *58*, 2634–2645.
[28] J. Kruszewski, T. M. Krygowski, *Tetrahedron Lett.* **1972**, *13*, 3839–3842.
[29] T. M. Krygowski, M. K. Cyrański, *Chem. Rev.* **2001**, *101*, 1385–1420.
[30] Z. Chen, C. S. Wannere, C. Corminboeuf, R. Puchta, *Chem. Rev.* **2005**, *105*, 3842–3888.
[31] C. M. Cardona, W. Li, A. E. Kaifer, D. Stockdale, G. C. Bazan, *Adv. Mater.* **2011**, *23*, 2367–2371.
[32] H. Tanaka, Y. Inoue, T. Mori, *ChemPhotoChem* **2018**, *2*, 386–402.
[33] T. Mori, *Chem. Rev.* **2021**, *121*, 2373–2412.
[34] Q. Zhou, W. Yuan, Y. Li, Y. Han, L. Bao, W. Fan, L. Jiao, Y. Zhao, Y. Ni, Y. Zou, H.-B. Yang, J. Wu, *Angew. Chem. Int. Ed.* **2024**, *63*, e202417749.
[35] X. Xiao, S. K. Pedersen, D. Aranda, J. Yang, R. A. Wiscons, M. Pittelkow, M. L. Steigerwald, F. Santoro, N. J. Schuster, Nuckolls C., *J. Am. Chem. Soc.* **2021**, *143*, 983–991.
[36] B. Liu, M. Böckmann, W. Jiang, N. L. Doltsinis, Z. Wang, *J. Am. Chem. Soc.* **2020**, *142*, 7092.
[37] W. Niu, Y. Fu, Q. Deng, Z.-L. Qiu, F. Liu, A. A. Popov, H. Komber, J. Ma, X. Feng, *Angew. Chem. Int. Ed.* **2024**, *63*, e202319874.
[38] W. Niu, Y. Fu, Q. Deng, Z.-L. Qiu, C. J. Schürmann, S. Obermann, F. Liu, A. A. Popov, H. Komber, J. Ma, X. Feng, *J. Am. Chem. Soc.* **2023**, *145*, 26824–26832.
[39] P. Izquierdo-García, J. M. Fernández- García, S. M. Rivero, M. Šámal, J. Rybáček, L. Bednarová, S. Ramírez-Barroso, F. J. Ramírez, R. Rodríguez, J. Perles, D. García-Fresnadillo, J. Crassous, J. Casado, I. G. Stará, N. Martín, *J. Am. Chem. Soc.* **2023**, *145*, 11599.
[40] L. Arrico, L. Di Bari, F. Zinna, *Chem. - Eur. J.* **2021**, *27*, 2920–2934.

Manuscript received: January 15, 2025
Revised manuscript received: March 02, 2025
Accepted manuscript online: March 09, 2025
Version of record online: March 18, 2025